Proof of concept of 35 kW electrical taxiing system in more electrical aircraft for energy saving

Hassan Cheaito, Bruno Allard, Guy Clerc

Proof of concept of 35 kW electrical function for embedded system in MEA for energy saving

Hassan Cheaito, Bruno Allard and Guy Clerc

Univ Lyon, INSA Lyon, Univ Claude Bernard, Ecole Centrale Lyon, CNRS, F-69621 Villeurbanne, France

Abstract

In the More Electric Aircraft (MEA), many subsystems that previously used hydraulic, mechanical, and pneumatic power have been fully or partially replaced with electrical systems. Particularly, this paper proves the feasibility of an equipment intended for the electric taxiing. Namely the design of a 35 kW DC-DC converter with 2500 Wh storage unit targets the recovery of energy from aircraft electrical brake and restitution on the network. First, the main technical and electrical characteristics of the converter prototype are described. The design of the battery pack is detailed. A 35kW interleaving multilevel converter appears to be a good candidate to fit with the aeronautic constraints. The total mass of such equipment is 68 kg while volume is 72 L.

Keywords: Electric Taxiing (ET), Energy Storage System (ESS), Lithium-ion Battery (LIB) and Bidirectional converter (BDC).

1. INTRODUCTION

EXPERTS believe that global air traffic is expected to increase dramatically since one central scenario foresees a doubling of passenger numbers in many developing countries by 2035 [1, 2]. Undoubtedly, this evolution will have a harmful impact on the environment such as increasing the CO_2 and NO_x emissions. Indeed, the aviation sector still largely relies on fossil fuels. Therefore, in order to achieve operating improvements as well as reducing costs and environmental impact, the transition to more electrified aircraft (MEA) systems is

being explored [3, 4, 5].

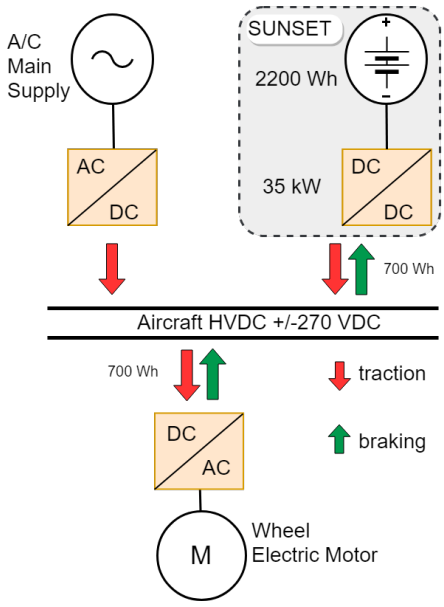

Figure 1: Schematic of the SUNSET within the aircraft network

Until today, before taking-off, a tractor has to push-back the aircraft from the gate to be ready on the tarmac. Then, the crew starts the engine to move the aircraft forward to the landing runway in a procedure known as *taxiing*. In some cases, taxiing operations can take over 30 minutes [6]. During taxiing, huge aircraft engines designed for flight phases at high power levels are used as a power source. As a result, using the main engines for on ground operations leads to increased fuel burn as the systems are forced to operate in highly inefficient conditions. Fuel consumption from aircraft taxiing is forecast to cost 7 billion dollars and accounts for an average of 18M metric tons of CO2 emission per year [7]. In fact, this idea is the motivation for the present work: instead of using its main engines for taxiing on airport taxiways, burning fuel unnecessarily, the aircraft will use small onboard electric motors to drive the wheels. This would allow the main engines to remain switched off until shortly before take-off. As a result, electric taxiing (ET) would save about 4% in fuel consumption and

achieve a significant reduction in carbon emissions (CO_2, NO_x, CO, etc.) [6, 8]. In addition, the ET system will allow aircrafts to push back without any support from an external tug. Thus, the aircraft will be more autonomous, i.e. able to reverse and depart its stand more quickly without relying on ground services and infrastructure. This solution helps improving traffic flows at gates and flight punctuality by gaining precious minutes on the ground, thereby contributing to maximizing the capacity of airports. Finally, yet importantly, using electric brake (while taxiing) instead of mechanical one would improve lifetime of the aircraft wheel and the brake system used during the landing phase.

Much research has been conducted in the context of More Electric Aircraft (MEA) and many projects have been undertaken, which resulted in the deployment of large number of electrical devices in large civil aircrafts by Airbus and Boeing [5, 9, 10]. However, to the best knowledge of the authors, this is the first paper who describes design and sizing of an electrification function from the system-level point of view. This paper extends with deep details an earlier conference paper describing a new project of Storage energy UNit for Smart and Efficient operation on Tarmac (SUNSET) [11]. As shown in Fig. 1, the power unit of electric taxiing, SUNSET in other words, includes both Electric Storage System (ESS) and power converter. Being installed onboard, electric motors provides the opportunity to recover the energy while braking, an issue which has been widely developed in the electric vehicles [12, 13]. Therefore, the SUNSET demonstrator should be able to do both: supply the electric motor with energy during traction and recover energy during braking (see Fig. 1).

The weight of an aircraft such as the A320 could be 70 Tons on average [14] and the maximum velocity allowed on the tarmac is around 30 km/h (8.3 m/s). So, the amount of involved energy should be roughly 0.5 mV^2 = 0.5 (7 x 104 x 8.3^2) = 2430 kJ = 675 Wh. Meaning that the maximum energy that the ESS should be able to recover is about 700 Wh during a final breaking. If around 35 seconds are considered as necessary to totally stop the aircraft at half the available kinetic energy, the power of the ESS should be P=E/t = 350 Wh /35 sec = 36000 W $\simeq$ 35 kW. These two quantities (power and energy) make the

preliminary specifications that determine later the weight and the volume of SUNSET. For instance, under 540 VDC, the current handled by the converter should be (35 kW/540 V) 65 A: a value that is going to be very significant for the sizing of the input filter against electromagnetic compatibility (EMC) or the power transistors.

This paper describes the hardware design of the SUNSET equipment. Not only does it show the feasibility study of such a demonstrator but also the preliminary experimental results. The design of this equipment is very challenging because, in addition to the high power and energy densities, it should also meet all the specifications of DO-160 standards such as safety, vibration stress, EMC, etc. Obviously, the key parameter in the sizing of such equipment would be the ESS. For this reason, the next Section will discuss the best candidate of storage technologies to be considered. In Section III, the converter topology and technology of the power board are highlighted. Experimental results are presented for the buck mode of the converter ending by the figure of merit of the prototype. Finally, a few concluding remarks are drawn in Section IV.

2. ELECTRIC STORAGE SYSTEM: BATTERY PACK

This Section discusses the choice of batteries within the three main storage technologies [15]: Supercapacitors (SC), Lithium-ion batteries (LIB) and Lithium-ion Capacitors (LIC).

2.1. State of the Art

While lead acid cells [16] store and release energy via a redox reaction, LIBs use intercalation, i.e. inserting lithium ions into the crystal lattice structure of the electrodes [17]. In the literature, the term "Lithium-ion battery" is widely used when the Li^+ ion is elaborated in the cell. Depending on the choice of materials and combinations of the two electrodes, the voltage, the energy density, the lifespan and the safety of a LIB can change dramatically. In this context, the major commercialized technologies are: Lithium Cobalt Oxide

(LCO), Lithium Manganese Oxide (LMO), Lithium Nickel-cobalt-Aluminium oxide (NCA), Lithium Nickel Manganese Cobalt Oxide (NMC), Lithium Iron Phosphate (LFP) and Lithium Titanium Oxide (LTO) [18, 19]. In contrast to batteries, supercapacitors (SC) have electrodes made of active materials such as the activated carbon that adsorbs ions present in the electrolyte. The charge is then stored by an electrostatic process rather than a faradaic one. Compared to LIBs, main advantages of SCs are their long lifecycle and high power density. However, their auto-discharge rates are high and their energy densities are low [20]. A new technology that combines both conventional ESSs (SCs and LIBs) is the Lithium-ion Capacitors (LIC). The target of this component is to fill the gap between low energy density of SCs and low power density of LIBs [21]. Several LIC technologies exist. For one of them, JSR Micro for instance, the positive electrode is similar to the positive electrode of a SC. Similarly, the negative electrode of an LIC is the same as the one of LIBs [22]. Fig. 2 compares the SUNSET's targets densities (2 kW/kg; 60 Wh/dm^3) to those of three representative types of ESSs according to the suppliers' datasheet. Of course, there are plenty of products and manufacturers but the aim is to compare the order of magnitude of three main types of ESSs. The SC technology can deliver high power ($\simeq$ 10 kW/kg) but only for a short period of time implying low energy supply ($\simeq$ 7 Wh/dm^3). The LIC can store more energy ($\simeq$ 30 Wh/dm^3) but not enough yet to reach the SUNSET target. However, the LIB easily reaches the energy target ($\simeq$ 300 Wh/dm^3) and for some battery technologies, it can provide the needed power ($\simeq$ 2 kW/kg). For this reason, SC and LIC have not been considered so far. In addition, having more energy in the pack (typically 200 Wh/dm^3 vs 60 Wh/dm^3 as target) is beneficial to improve LIB performance.

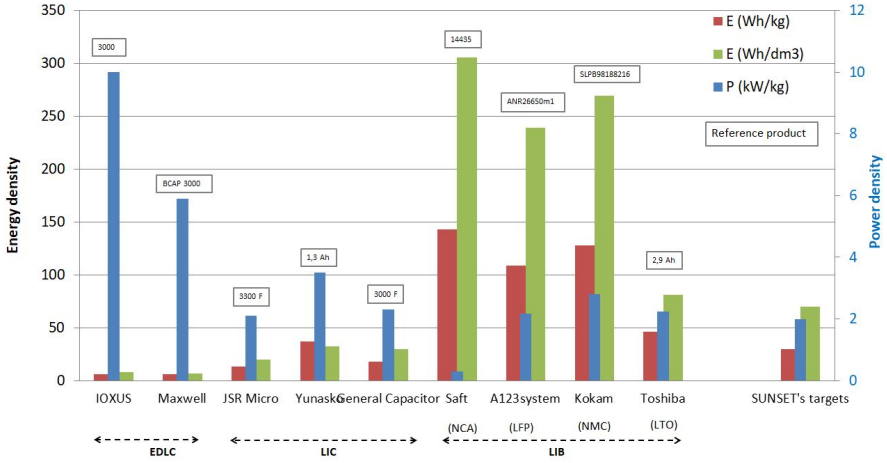

Figure 2: Power and energy densities according to the market suppliers

However, designers have to be careful about the values released in datasheets and need to figure out in what conditions the tests have been performed (temperature, duration, SoC, rest...) for the following reasons :

1. Sometimes, the power density is given for the maximum current over a short time (e.g. 1 s or 10 s). That's why there are in datasheets higher density values than the ones reflected here. However, the former values are not useful except for a short duration which is not the application case here.
2. In some cases, the maximum current or the C-rate is higher in discharge than in charge. The power density is given with respect to the highest current to be delivered, which is not totally accurate. For example, the Kokam's products have typically a discharge C-rate around 20 whereas only 1C in charging (SLPB 8043128H [23]).
3. Working at the highest current is feasible from the cell viewpoint. But one should verify if, by taking into account the losses due to the Equivalent Series Resistance (ESR), the efficiency of the battery pack is still worthy.

Based on a previous trade-off analysis [11], the cylindrical A123 system cell (2.5 Ah; 3.3 V) has shown a very competitive energy density (240 Wh/L and

108 Wh/kg). Furthermore, LFP cells provided by A123 system have shown a good capability with respect to environmental conditions and qualifications for aeronautic applications. The following subsection presents in details the ESS (35 kW, 700 Wh) packaging based on the ANR26650 LFP cell (72 g; 0.0344 dm^3).

2.2. Electric Performances

The ESR has been extrapolated from the datasheet at 35 °C for different SoC values [24]. First, the preliminary sizing is done according to fixed values (nominal voltage and current) regardless of the SoC. Second, several iterations should be done to re-verify power capability and current limit considering ESR and Open Circuit Voltage (OCV) at different SoC value. It is worth noting that the cell has asymmetric characteristics, i.e. the maximum allowable current in discharge is higher than the charge current, similar for ESR. Assuming that the maximum allowable current in charge discharge at 35 °C is 35 A (14C) for 50 seconds, the following sizing could take place:

- U = P/I= 35000/35 = 1000 V. In practice, instead of energizing from one branch, it is more convenient to share the power over several branches. In this case, three branches of 333V are put in parallel in order to supply of the total power with more current and less voltage.
- Number of cells N = U_{branch}/U_{cell} = 333/3.3, that leads approximately to 100 cells per branch noted as 3p100s (i.e. 3 parallel branches of 100 cells in series). Meaning that the total current handled by the branches is 105 A.
- Weight = 0.072*100*3 = 22 kg for the 3p100s configuration
- Volume = 0.0344*100*3 = 10 dm^3
- Embedded Energy = I (Ah)*U_{cell} (V)*N = 2.5*3.3*100*3 = 2500 Wh

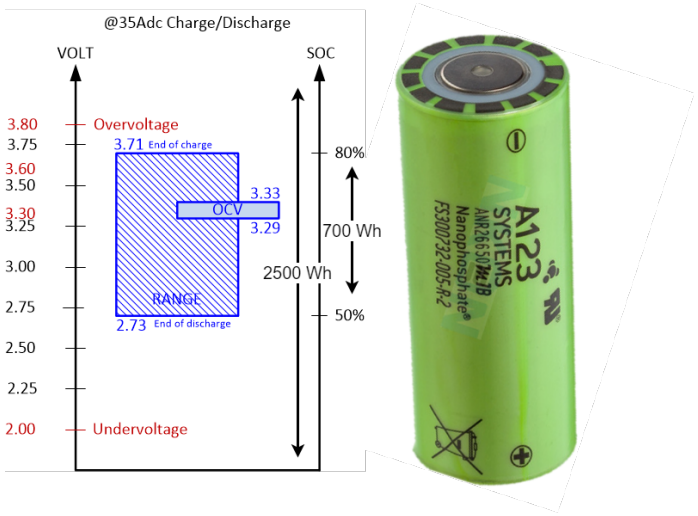

Figure 3: The OCV as function of SoC for A123 System cell

Obviously, the energy stored in the pack (2500 Wh) is three times higher than the target (700 Wh), but that is quite reasonable to avoid reaching the Depth of Discharge (DoD) of 100%. Staying in the comfort zone of the cell (dashed zone in Fig. 3), i.e. SoC between 50% and 80%, will extend the life cycle of the cells and would slow down the aging caused by the high current used (14C).

2.3. Aging

In fact, the SUNSET application follows a special profile, i.e. the cells, at 35 °C ambient temperature, are highly stressed (charging and discharging at 14C) during a short time (taxiing). Then, they stay at rest for a few hours (during flights) and so on. Unfortunately, using the datasheets the life cycle may not be estimated because they are performed under non similar conditions. That is why a representative profile (Fig. 4) has been performed on one cell in order to investigate the performance of the ESS. Using an Arbin Battery Testing Unit (BT2000) and a Votsch instrument (VC4018), the cell is charged by a Constant Current (CC) of 35 A for 50 s succeeded by -35 A after a rest time for 5 min. As shown in Fig. 4, one cycle is defined at the end of the discharging phase. Fig. 5 plots the life cycle which shows more than 5000 cycles

above 83% of nominal capacity. This is helpful information because aircraft manufacturers could estimate the lifetime of such a demonstrator depending on the daily cycles. More information about aging on the same cell can be found in [25, 26, 27].

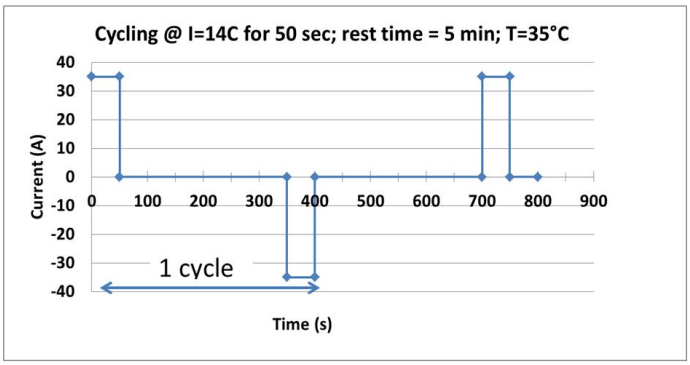

Figure 4: Profile admitted for the SUNSET application

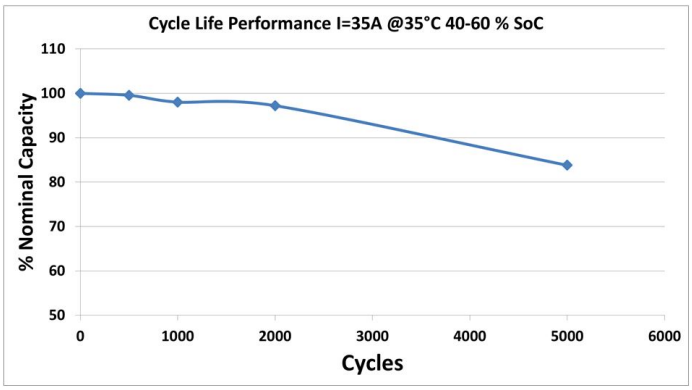

Figure 5: Aging of A123 System cell : 5000 cycles according to Fig. 4

2.4. Mechanical design

To build the energy storage system (ESS), the mechanical design will be based on the smallest unit which is the cell. Each 20 cells are packaged in series into one module (see Fig. 6. Each 5 modules in series constitute one pack. For each pack (100 cells in series), there is one Battery Management System (BMS) board and one Solid State Power Control (SSPC) board. The total ESS of the SUNSET equipment comprises three packs. At each packaging level, the energy

densities are evaluated. Fig. 6 shows how densities are highly decreasing from the cell level to the pack level. For instance, at the pack level the volume density drops down to 69 Wh/L instead of 240 Wh/L at the cell level. The mass density decreases to 67 Wh/kg whereas firstly it was 108 Wh/kg. On the one hand, these successive deratings in volume and mass density are due to the minimum spacing between cells, air corridor (expected for cooling) and the mechanical housing of the modules and packs (aeronautic constraints). On the other hand, the strip connexion between cells and the addition of BMS and SSPC at the pack level decrease some more the densities of the overall design. It is worth to note that the SSPC has been validated to open a short circuit current of 350 A. However, for the sake of place, the SSPC will not be discussed here.

Indeed, from the latter results, it comes that the design should consider about 70% and 40% (in volume and mass respectively) of derating between the initial energy density of the cell and the one of the final, fully integrated pack. From this angle, the cylindrical cell seems to be less beneficial than prismatic or pouch ones. However, the final values of density still meet the product target.

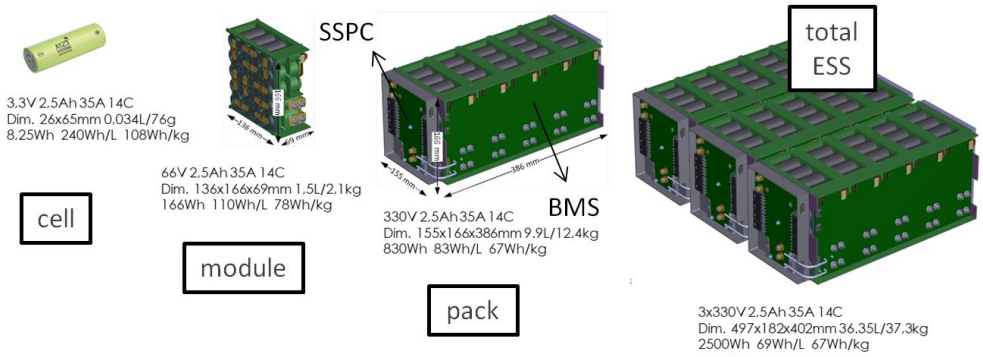

Figure 6: Evolution of the mechanical design of the SUNSET ESS: densities decrease dramatically from one cell to the total ESS (70% for the energy volume density and 37% for the mass density)

2.5. Thermal Management

The cooling system is based on forced air ventilation (no water cooling authorized). The cooling system is designed based on calculations and simulations from typical operation profiles and electrical losses in the overall system at a specified ambient temperature of 35 °C. The control of ESS temperature is the most critical because of the high losses and the high thermal inertia, i.e. once heated, it takes a long time for it to lose heat. The battery temperature should be controlled within temperature limits to avoid the thermal runaway, guarantee the estimated life cycle and maintain the same performance. The simulation shows that, in order to limit the absolute temperature to 60 °C, an air flow equal to 400m^3/hr is required. Under the assumption of uniformity, each battery module would have an air flow of 26 m^3/hr. Fig. 7 shows a simulation of one battery module following a typical profile of charging/discharging using 6SigmaET software [28]. The ambient temperature is set to 35 °C and the air flow is 26 m^3/hr. As shown, a maximum temperature of 60 °C is evaluated.

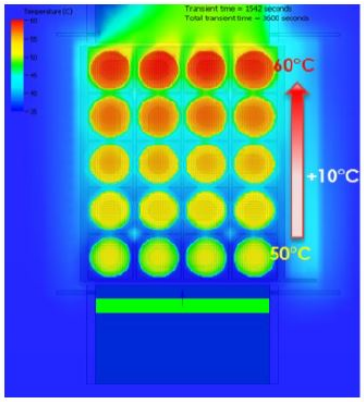

Figure 7: Simulation of one battery module considering the air flow of 26 m^3/hr

3. DC-DC CONVERTER

This Section discusses the power converter architecture compatible with a nominal power of 35 kW.

3.1. Topology

The HVDC network of the aircraft, typically 540VDC, is a balanced symmetrical bus having a voltage between +270V and -270V. The designed DC-DC power converter is a two-level voltage converter based on the midpoint of the HVDC network. The first objective of this topology is to reduce voltage constraints on semiconductor devices, allowing to lower switching losses [29]. Another objective is to minimize voltage constraints on magnetic devices, namely inductors and the capacitors, which helps to integrate them on PCB due to low form factors [30]. Thus, the main input voltage (540V) is divided into two legs of 270V each. As can be seen in Fig. 8, the converter contains six legs (blue dashed rectangle). Each two legs constitute one phase. Moreover, three interleaved phases are connected to the three battery branches. The switching frequency is chosen to be 46 kHz to set the first harmonic below EMC limits. Table presented in Fig. 9 shows the switching strategy: a 120° phase delay is applied between the three interleaved phases. Indeed the first harmonic seen by the HVDC network (below 140 kHz) is related to the number of phases. The EMC filter is dimensioned based for 140 kHz operating frequency, which is the highest value for a good industrial trade-off with respect to DO-160. Furthermore, the converter should be bidirectional: it recovers energy during braking and operates as in buck mode ($540\,\mathrm{V} \mapsto 330\,\mathrm{V}$), then discharges batteries during traction and operates as in boost mode ($330\,\mathrm{V} \mapsto 540\,\mathrm{V}$). In order to obtain reversibility, the conventional diodes in the half-bridge buck are replaced by a second transistor to design a boost converter. Besides, a galvanic isolation is not necessary because the battery pack offers a floating voltage source. In summary, the adopted topology is a bidirectional DC-DC synchronous buck converter composed of two levels and three interleaved phases.

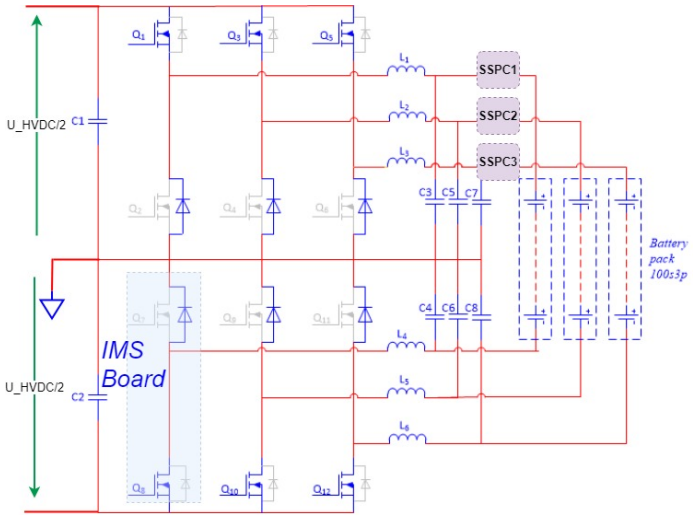

Figure 8: Architecture of the converter within the overall design

	PERIOD / SWITCH	[0;T/3]	[T/3;2T/3]	[2T/3;T]
PHASE 1	Q1/Q8	ON	ON	OFF
	Q2/Q7	OFF	OFF	ON
PHASE 2	Q3/Q10	OFF	ON	ON
	Q4/Q9	ON	OFF	OFF
PHASE 3	Q5/Q12	ON	OFF	ON
	Q6/Q11	OFF	ON	OFF

Figure 9: Switching with 120° phase shift between the three phases

3.2. PCB design

Over the past decade, SiC power devices have been widely deployed for various power electronics applications since they have proven superior performance and maturity over their Si counterparts [31]. In particular, SiC MOSFETs are spread more and more for high-voltage applications because of their low on-state resistance, fast switching, and high-temperature operation capability [32, 33, 34]. Besides, in order to reduce EMI issues, kelvin connections are highly recommended. Leadless or low-lead components are preferred as well to

reduce parasitic inductance. In addition, SMD MOSFETs provide easier soldering and wiring from the industrial point of view. For these reasons, D^2-PAK (SCTH90N65G2V) has been chosen for this application. Nowadays, Insulated Metal Substrate (IMS) technology is increasingly being used in power electronics for its excellent heat transfer properties [35]. The IMS board also privileges SMD components for more compact designs. As mentioned earlier, the SUNSET converter contains six legs. They are implemented using six IMS boards (blue dashed rectangle in Fig. 8). Each switch in the half-bridge is a two-parallel-chip transistor. As shown in Fig. 10, one separate driver board is stacked on the top of those six IMS boards and connected via jumper to control the MOSFETs. However, the IMS board has a strong influence on the EMC, namely at the routing level. Indeed the proximity of tracks to a large conductive surface allows minimizing their inductive effects, but this leads to a larger common-mode capacitance. In which case routing becomes a key point for obtaining a circuit with good performances. The floating node area must be as small as possible to limit the common-mode capacitance. The symmetry of the circuit is extremely important to avoid common-mode to differential-mode conversion [36, 37]. The current design of the power converter based on this technology gives a final power density of 3 kW/kg (including inductors and heatsink).

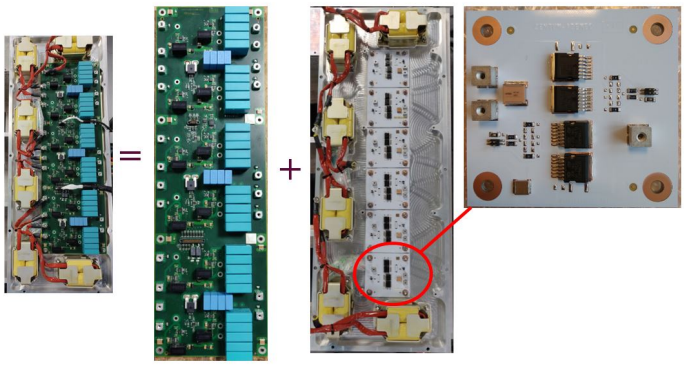

Figure 10: Picture of the DC-DC bidirectional converter showing one driver board, six inductors and six IMS boards

3.3. Validation test of the elementary power unit

This Section presents the electrical performance (switching, losses, and nominal power) of the elementary half-bridge circuit (one IMS board). For the sake of place, only the results for the high-side MOSFET in buck mode are presented. A comparison is carried out between analytical study and experimental measurement following the operating conditions in table presented in Fig. 11.

SWITCHING FREQUENCY	50 kHz	V INPUT	325 V
DUTY CYCLE	0.6	I OUTPUT	30 A
POWER	5.85 kW	LOAD	6.3 Ω

Figure 11: Operating conditions of the elementary board

3.3.1. Theoretical study

Total losses in MOSFETs are predicted according to a theoretical analysis. Only the final results are shown according to the calculation shown in (5) and detailed in [38]. This allows evaluating the distribution of losses between switching and conduction modes. The losses are estimated to be 11.9 W distributed as shown in Fig. 12.

$$P_{total} = P_{cond} + P_{SW} + P_{rr} + P_{gate} \tag{1}$$

Where:

- P_{cond} : conduction losses
- P_{SW}: switching losses (on and off)
- P_{rr}: reverse recovery losses
- P_{gate}: gate-drive losses

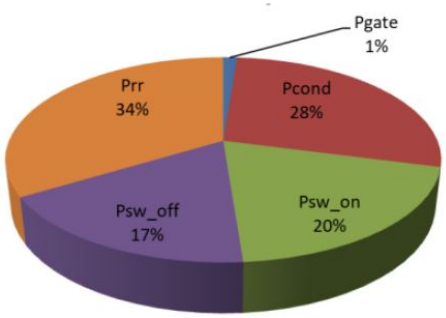

Figure 12: Losses in the high-side MOSFET on the elementary power board

3.3.2. Experimental Results

Tests in buck-mode have been performed at the maximum power of 5.85kW. The same conditions in Table II have been considered. The switching frequency is set to 50 kHz and the duty cycle to 60%. The dead time is set to 500 ns. The curves in Fig. 13 show V_{GS} (yellow) and V_{DS} (green) during the turn-off of the low side transistors. These measurements validate the design of the IMS board. The gate voltage (V_{GS}) does not exceed the minimum threshold of 1.9 V; i.e. no false turn-on could happen. Besides, the V_{DS} overvoltage is limited to 400V which is lower than V_{BR} of MOSFET (650 V). In order to validate the estimated losses in the previous section, it was necessary to carry out thermal tests. The thermal resistance (R_{th-IMS}) is calculated first for the IMS PCB, then it is calculated including the heatsinks in order to determine the global R_{th}. A series of tests has been conducted using the MOSFETs in the saturation operating region ($V_{GS} < 10V$) to control the injected power. The R_{th} is afterwards deduced readily from the ratio of temperature elevation over the dissipated power. The R_{th} effective value is about 1.65°C/W for the overall board including the heatsink. Once R_{th} is determined, the same switching conditions as in the previous Section are applied. Temperature elevation (ΔT) has been measured to be 20.5°C. This means that the power losses using thermal measurements are equal to 12.1 W ($\Delta T/R_{th}$). Fig. 14 shows the elevation of temperature at IMS surface. Notice that the highest temperature point is 48.7°C whereas the ambient temperature is 28.3°C. A good agreement has been found

between theoretical and experimental evaluations, which validate the design of the converter.

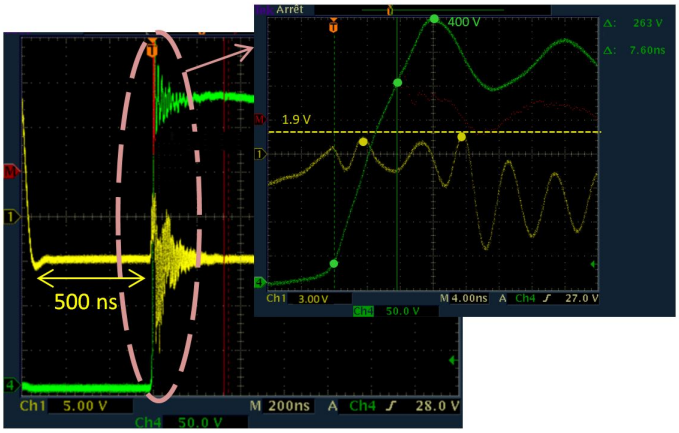

Figure 13: Waveforms on the high-side MOSFET on the elementary board: VGS (yellow) and VDS (green)

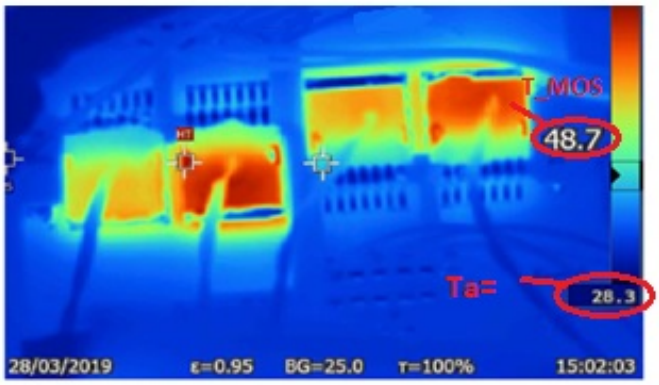

Figure 14: Infrared camera picture of the elementary power showing ambient temperature at 28°C and 48.7°C as the temperature of MOSFET

The total volume and weight of the SUNSET are 72 dm3 and 68 kg respectively. For further details, each functional block has been weighted as shown in the Fig. 15. It can be seen that the heaviest and most bulky part is the ESS.

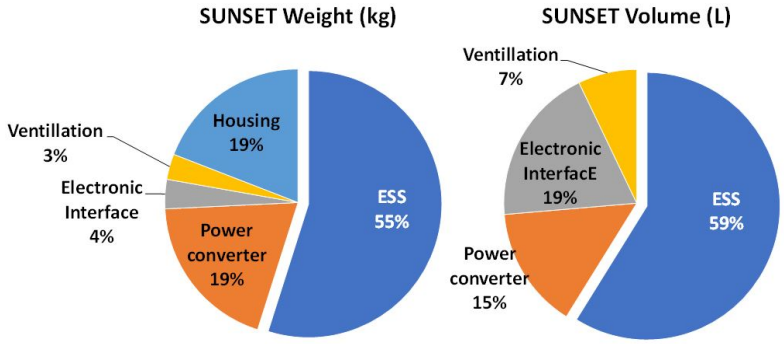

Figure 15: Repartition of mass and volume in the final prototype

4. Conclusion

This paper has discussed the SUNSET product from the system-level point of view. In addition, all described features could be used not only in the aeronautic domain but also in other contexts such as electric vehicles, solar systems, etc. This experimental work has validated a trade-off previously described in [11], and has shown the feasibility of such a demonstrator while presenting the obtained final densities. Those densities are highly regarded by designers in order to estimate the volume and mass of their electronic products. The following statements among others have been deduced:

1. The power and energy densities of a unitary cell in ESS is not significant. Study should take into account the packaging, BMS and protections. In our application, these added features have reduced the density to around 37% for the mass energy density and to 70% of the initial volume energy density.
2. A bidirectional DC-DC converter composed of two levels and three interleaved phases has been designed. IMS technology has been used in order to gain in densities: a density of 3 kW/kg including inductors and heatsink has been shown.
3. The heaviest and most bulky part in such a demonstrator is still the ESS. Further research shall be conducted in order to reduce the weight and

volume of the battery.

References

[1] T. Rutherford, Air transport statistics standard note: Sn/sg, 2011.

[2] International Air Transport Association Forecasts Passenger Demand to Double Over 20 Years. ([Online] Available : https://www.iata.org/en/pressroom/pr/2016-10-18-02; Accessed: 18-Mar-2020).

[3] K. Ni, Y. Liu, Z. Mei, T. Wu, Y. Hu, H. Wen, Y. Wang, Electrical and electronic technologies in more-electric aircraft: A review, IEEE Access 7 (2019) 76145–76166. doi:10.1109/access.2019.2921622.

[4] J. Jiang, M. Zhao, Z. Wen, C. Zhang, R. Albarracín, Detection of DC series arc in more electric aircraft power system based on optical spectrometry, High Voltage 5 (1) (2020) 24–29. doi:10.1049/hve.2019.0068.

[5] S. N. Motapon, L. A. Dessaint, K. Al-Haddad, A Comparative Study of Energy Management Schemes for a Fuel Cell Hybrid Emergency Power System of More Electric Aircraft, in: IEEE Transactions on Industrial Electronics, Vol. 61, pp. 6148–6156, 2014. doi:10.1109/TIE.2014.2308148.

[6] Safran Landing Systems - electric taxiing ([Online] Available: https://www.safran-landing-systems.com/systems-equipment/electric-taxiing-0. [Accessed: 19-Mar-2020]).

[7] Y. Jung, Fuel Consumption and Emissions from Airport Taxi Operations, NASA Ames Research Center - Green Aviation Summit.

[8] B. Sarlioglu, C. T. Morris, More Electric Aircraft: Review, Challenges, and Opportunities for Commercial Transport Aircraft, in: IEEE Transactions on Transportation Electrification, Vol. 1, pp. 54–64, 2015. doi:10.1109/TTE.2015.2426499.

[9] W. Zuo, R. Li, C. Zhou, Y. Li, J. Xia, J. Liu, Battery-supercapacitor hybrid devices: Recent progress and future prospects, Advanced Science 4 (7) (2017) 1600539. doi:10.1002/advs.201600539.

[10] C. Requirements, S. G, S. member, IEEE, A. K. Rathore, S. member, IEEE, D. M. Fulwani, Member, IEEE, Discontinuous conduction mode three phase buck- boost derived pfc converter for more electric aircraft with reduced switching, sensing and, IEEE, 5386.

[11] H. Cheaito, B. Allard, G. Clerc, P. Venet, A. Sari, P. Pommier-Petit, J. Pallier, Preliminary design of energy storage system and bidirectional dc-dc converter for aircraft application, in: 2019 IEEE 28th International Symposium on Industrial Electronics (ISIE), 2019, pp. 2547–2552.

[12] Development of a hybrid flywheel/battery drive system for electric vehicle applications, IEEE TRANSACTIONS ON VEHIC UL.AR TECHNOLOGY, VOL. V T - 2 6 . NO. 2 . h I A Y, 1977.

[13] G. Xu, K. Xu, C. Zheng, X. Zhang, T. Zahid, Fully Electrified Regenerative Braking Control for Deep Energy Recovery and Safety Maintaining of Electric Vehicles, in: IEEE Transactions on Vehicular Technology, Vol. 65, pp. 1186–1198, March 2016. doi:10.1109/TVT.2015.2410694.

[14] AIRBUS, Aircraft characteristics airport and maintenance planning, Tech. Rep. Services (2005).

[15] M. Farhadi, O. Mohammed, Energy storage technologies for high-power applications, IEEE Transactions on Industry Applications 52 (3) (2016) 1953–1961. doi:10.1109/tia.2015.2511096.

[16] P.-H. Huang, J.-K. Kuo, C.-Y. Huang, A new application of the Ultra-Battery to hybrid fuel cell vehicles, in: International Journal of Energy Research, Vol. 40, 2016, pp. 146–159. doi:10.1002/er.3426.

[17] S. Chauque, F. Y. Oliva, A. Visintin, D. Barraco, E. P. Leiva, O. R. Cámara, Lithium titanate as anode material for lithium ion batteries:

Synthesis, post-treatment and its electrochemical response, in: Journal of Electroanalytical Chemistry, Vol. 799, Elsevier, 2017, pp. 142–155. doi:10.1016/j.jelechem.2017.05.052.
URL http://dx.doi.org/10.1016/j.jelechem.2017.05.052

[18] M. A. Hannan, M. M. Hoque, Y. Yusof, K. Pin Jern, State-of-the-Art and Energy Management System of Lithium-Ion Batteries in Electric Vehicle Applications : Issues and Recommendations, IEEE Access 6 (2018) 19362–19378. doi:10.1109/ACCESS.2018.2817655.

[19] T. Horiba, Lithium-Ion Battery Systems, in: Proceedings of the IEEE, Vol. 102, IEEE, pp. 939–950, June 2014. doi:10.1109/JPROC.2014.2319832.

[20] A. Burke, Ultracapacitor technologies and application in hybrid and electric vehicles, in: International journal of energy research, Vol. 31, 2007, pp. 135–147. arXiv:arXiv:1011.1669v3, doi:10.1002/er.

[21] N. E. Ghossein, A. Sari, P. Venet, Nonlinear Capacitance Evolution of Lithium-Ion Capacitors Based on Frequency- and Time-Domain Measurements, in: IEEE Transactions on Power Electronics, Vol. 33, pp. 5909–5916, July 2018. doi:10.1109/TPEL.2017.2745716.

[22] N. El Ghossein, A. Sari, P. Venet, Effects of the Hybrid Composition of Commercial Lithium-Ion Capacitors on Their Floating Aging, IEEE Transactions on Power Electronics 34 (3) (2019) 2292–2299. doi:10.1109/TPEL.2018.2838678.

[23] Kokam company ([Online] Available: http://kokam.com/cell/. [Accessed: 20-Nov-2018]).

[24] Kokam company ([Online] Available: http://a123batteries.com [Accessed: 20-Jan-2019]).

[25] C. G. G.-D. C. S. Westenhover, D. A. Wetz, M. J. Martin, D. A. Dodson, John Heinzel, Current Sharing in Parallel Cell Batteries Cycled at High

C Rates, in: 2017 IEEE Electric Ship Technologies Symposium (ESTS), Arlington, VA, 2017, pp. 586–591.

[26] D. A. Wetz, B. Shrestha, S. T. Donahue, D. N. Wong, M. J. Martin, J. Heinzel, Capacity fade of 26650 lithium-ion phosphate batteries considered for use within a pulsed-power system's prime power supply, IEEE Transactions on Plasma Science 43 (5) (2015) 1448–1455. doi:10.1109/TPS.2015.2403301.

[27] B. M. Huhman, J. M. Heinzel, L. Mili, C. T. Love, D. A. Wetz, Investigation into State-of-Health Impedance Diagnostic for 26650 4P1S Battery Packs, Journal of The Electrochemical Society 164 (1) (2017) A6401–A6411. doi:10.1149/2.0631701jes.

[28] 6SigmaET, Intelligent Thermal Simulation For Electronics ([Online] Available: https://www.6sigmaet.info/. [Accessed: 20-Apr-2020]).

[29] A. A. Khan, H. Cha, H.-g. Kim, A Family of High Efficiency Bidirectional DC-DC Converters Using Switching Cell Structure, 2016 IEEE 8th International Power Electronics and Motion Control Conference (IPEMC-ECCE Asia) (2016) 1177–1183doi:10.1109/IPEMC.2016.7512455.

[30] H. Abu-Rub, J. Holtz, J. Rodriguez, G. Baoming, Medium-voltage multilevel converters State of the art, challenges, and requirements in Industrial applications, IEEE Transactions on Industrial Electronics 57 (8) (2010) 2581–2596. doi:10.1109/TIE.2010.2043039.

[31] L. Wu, J. Qin, M. Saeedifard, O. Wasynczuk, K. Shenai, Efficiency evaluation of the modular multilevel converter based on si and SiC switching devices for medium/high-voltage applications, IEEE Transactions on Electron Devices 62 (2) (2015) 286–293. doi:10.1109/ted.2014.2375875.

[32] D. Liu, Y. Wang, F. Deng, Q. Zhang, Z. Chen, Zero-Voltage Switching Full-Bridge T-Type DC/DC Converter with Wide Input Voltage Range

and Balanced Switch Currents, IEEE Transactions on Power Electronics 33 (12) (2018) 10449–10466. doi:10.1109/TPEL.2018.2800902.

[33] Y. nakakohara, H. Otake, T. Evans, T. Yoshida, M. Tsuruya, K. Nakahara, Three phase LLC series resonant DC/DC converter using SiC MOSFETs to realize high voltage and high frequency operation, IEEE Transactions on Industrial Electronics (2015) 1–1doi:10.1109/tie.2015.2499721.

[34] Q. Yan, X. Yuan, Y. Geng, A. Charalambous, X. Wu, Performance evaluation of split output converters with SiC MOSFETs and SiC schottky diodes, IEEE Transactions on Power Electronics 32 (1) (2017) 406–422. doi:10.1109/tpel.2016.2536643.

[35] E. Juntunen, A. Sitomaniemi, O. Tapaninen, R. Persons, M. Challingsworth, V. Heikkinen, Thermal performance comparison of thick-film insulated aluminum substrates with metal core PCBs for high-power LED modules, IEEE Transactions on Components, Packaging and Manufacturing Technology 2 (12) (2012) 1957–1964. doi:10.1109/tcpmt.2012.2206390.

[36] H. Cheaito, M. S. Diop, M. Ali, E. Clavel, C. Vollaire, L. Mutel, Virtual Bulk Current Injection: Modeling EUT for Several Setups and Quantification of CM-To-DM Conversion, IEEE Transactions on Electromagnetic Compatibility 59 (3) (2017) 835–844. doi:10.1109/TEMC.2016.2631721.

[37] X. Gong, I. Josifović, J. A. Ferreira, Modeling and reduction of conducted EMI of inverters with SiC JFETs on insulated metal substrate, IEEE Transactions on Power Electronics 28 (7) (2013) 3138–3146. doi:10.1109/tpel.2012.2221747.

[38] D. Graovac, M. Pürschel, K. Andreas, MOSFET Power Losses Calculation Using the Data- Sheet Parameters, Infineon Technologies AG (July) (2006) 1–23.
URL http://application-notes.digchip.com/070/70-41484.pdf